

We are IntechOpen, the world's leading publisher of Open Access books Built by scientists, for scientists

6,100

Open access books available

149,000

International authors and editors

185M

Downloads

Our authors are among the

154

Countries delivered to

TOP 1%

most cited scientists

12.2%

Contributors from top 500 universities



WEB OF SCIENCE™

Selection of our books indexed in the Book Citation Index
in Web of Science™ Core Collection (BKCI)

Interested in publishing with us?
Contact book.department@intechopen.com

Numbers displayed above are based on latest data collected.
For more information visit www.intechopen.com



Chapter

High-Temperature Operating Narrow-Period Terahertz Quantum Cascade Laser Designs

Li Wang and Hideki Hirayama

Abstract

Presently, terahertz quantum cascade lasers still suffer from operations below room temperature, which prohibits extensive applications in terahertz spectra. The past continuous contributions to improving the operating temperatures were by clarifying the main thermal degradation process and proposing different designs with the optical gain demonstrating higher temperature cut-offs. Recent designs have attempted to employ a narrow period length with a simplified and clean state system, and reach renewed operating temperatures above 200 K. This study reveals how historic designs approach such narrow-period designs, discuss the limitations within those designs, and show further possible designs for higher operating temperatures.

Keywords: high operating temperature, terahertz, quantum cascade lasers, narrow-period design

1. Introduction

The terahertz (THz) electromagnetic spectrum ($\lambda \sim 600\text{--}30\ \mu\text{m}$, $\hbar\omega \sim 2\text{--}40\ \text{meV}$) remains the most underdeveloped spectral region, at least largely due to the lack of THz radiation sources with coherent or compact wave features and high output power. The potential for applications in THz spectra is included but is not limited to atmospheric science, astrophysics, biological/medical sciences, security screening and illicit material detection, nondestructive evaluation, ultrafast spectroscopy, and communications technology [1–4]. THz quantum cascade lasers (THz-QCLs) are thought to be the only solid-state THz sources that can offer average optical power levels much greater than milliwatts, which are profitable for imaging applications [5], and continuous-wave (CW) operation for the frequency stability desired in high-resolution spectroscopy techniques.

These laser sources escape the inherent prevention of the working principle of conventional lasers, which naturally relies on the bandgap of semiconductor materials to realize electron-hole recombination. In comparison, the THz photon energy has only several or tens of meV, which is inaccessible to interband transitions. THz-QCLs employ the quantum process of intersubband transitions (ISBT) within repeating superlattice period units [6]. The radiation frequency can be freely tuned solely by engineering the energy separations of dispersed quantum levels, for example, only in

the conduction band area. Rapid developments in THz-QCLs have been reported since their first realization in 2002 [5], with the 1.2–5 THz frequency coverage range (operated without the assistance of an external magnetic field [7–9]). Although the initial demonstration of THz-QCLs was performed with the aid of single-plasmon waveguide structures [5], the subsequent development of double-plasmon metal-metal waveguides [10] led to higher operating temperatures (T_{max}). Due to the subwavelength dimensions of the emitting aperture in metal-metal waveguides, their emission is characterized by divergent beam patterns and low output powers [11, 12]. However, unique distributed-feedback (DFB) techniques have recently been demonstrated to achieve single-mode operation with narrow beam patterns [13–15]. Until now, the main limitation for THz-QCL is that the operations suffer from serious thermal degradation, and a room temperature without additional cooling is still not reached. **Figure 1** shows a summary of the improvements in T_{max} over the past decades [16].

The main thermal degradations can be sorted into two types. The first type is the reduction of population inversions (Δn), which can be due to the reduction of population shares in the upper laser state (u, n_u), and an increasing trend at the lower laser state (l, n_l) as the temperature increases. The former can be mainly ascribed to the directly enhanced scattering of the LO-phonon. In general, the active region of the THz-QCL is based on GaAs semiconductor materials, and its LO-phonon energy ($E_{LO} \sim 35$ meV) is quite small. THz radiation is mostly designed below the LO-phonon energy. At high temperatures, the electrons in the upper laser state will acquire enough in-plane kinetic energy (E_{hot}) to relax down to the lower laser state by emitting LO-phonons ($E_{hot} + E_{ul} \approx E_{LO}$) instead of photon emission ($E_p \approx E_{ul}$) [17, 18]. In addition, the up-scatterings from the upper laser state into the higher energy states or directly over the barrier (in the case of low barrier structures) by absorbing the hot phonons [19, 20] lead to efficient carrier leakages. Both of these phonon-assisted processes significantly reduce the population shares in the upper laser state. In addition, the population share of the upper laser state is closely related to the injection efficiency, which can be significantly degraded by injection at high temperatures via

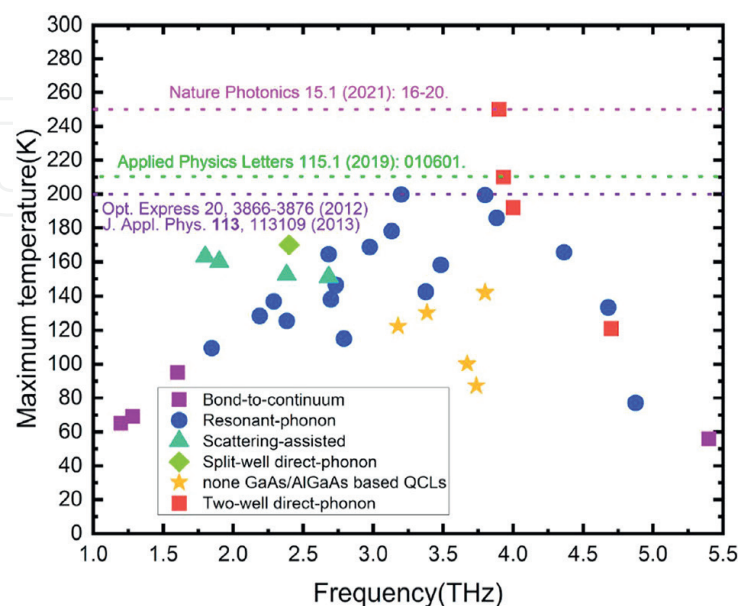


Figure 1. Survey of the best operating temperature T_{max} at various THz lasing frequency achieved based on different THz-QCL design within pulse operation mode, with the permission from Ref. [16].

resonant tunneling [10, 21]. This is because the resonant tunneling at the injector undergoes enhanced decoherence at high temperatures; as a result, more population is retarded at the injector, thus reducing the population share in the upper laser state. The latter can be thought of as a result of an increased lifetime of the lower laser state because the thermal backfilling from the injector areas is more serious at high temperatures [22, 23]. The second type of degradation is the thermal broadening of the radiation linewidth (Γ) in the active region, and the peak of optical gain is significantly decreased even when a large fraction of population inversion is maintained [24]. This broadening effect is primarily ascribed to the increased Coulomb scattering [25]. Meanwhile, Ref. [25, 26] also pointed out the importance of considering the correlation effect on those broadening for a self-consistent gain profile calculation, which can partially recover the gain peak. These degradation processes occur simultaneously, limiting the final optical gain ($g \sim \Delta n / \Gamma$) below the cavity threshold.

2. THz-QCL designs

The realization of high- T_{\max} THz-QCLs is indeed beneficial from the corresponding strategies for suppressing the thermal degradation in the active region and, simultaneously, trying to stabilize the real growth to consistently realize the designs. The multiple-quantum-well active region is usually grown using molecular-beam epitaxy in a GaAs/Al_xGa_{1-x}As material system and is the heart of any QC laser. To obtain the gain for electromagnetic waves at frequency ν , energy levels, wavefunctions, and scattering rates must be properly engineered to provide a population inversion between two states separated by energy $h\nu$. The basic innovation for the successful realization of a QCL can be ascribed to the introduction of the injector region. The optical gain from intersubband transitions in semiconductor superlattices was first investigated early in 1971 [27]; however, early laser proposals suffered from electrical instability owing to the formation of high-field domains crossing the stacked superlattices, until the injector region was particularly defined for offering an accessible operating bias condition, thus realizing the first QCL in the mid-infrared spectrum in 1994, as shown in **Figure 2** [28]. Next, the first THz-QCL lasing at 4.4 THz was experimentally demonstrated in 2002, where most innovations can be ascribed to semi-insulating surface plasmon (SISP) waveguides in the THz spectra [5]. Consequently, the injector has remained a common region in QCLs design for THz QCLs. It should be noted

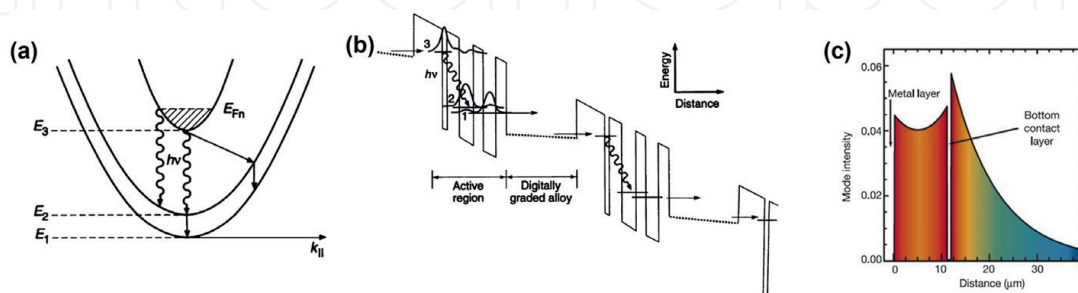


Figure 2. Schematic description of the three relevant levels where E_3 , E_2 , and E_1 stand for the upper-laser, lower-laser, and extractor states, respectively (a), the diagram of the band profile of cascading structures with neighboring periods under the operating applied bias, the extracted electrons will relax into the graded area and then reinjected into the upper-laser state in the next period by resonant tunneling (b), Ref. [28]; The semi-insulating surface plasmon (SISP) waveguide for realizing the first THz-QCL (c), where the bottom contact layer is a thin heavy doped GaAs (n^+ -GaAs) layer grown on an undoped GaAs substrate, Ref. [5].

that the performance of THz-QCLs is particularly sensitive to the injector because the small energy separation between the laser states makes it difficult to selectively inject carriers (electrons) into the upper laser state [29, 30]. Therefore, improving injection selectivity has gained much attention for different designs [31–33]. The detailed design parameters are trapped in trade-offs from one to another; a successful scheme always requires a dedicated balance of the different parameters.

The main design schemes in the past are shown in **Figure 3a** *chirped superlattice (CSL)*, as shown in **Figure 3a**. The CSL scheme is a main early design, and it employs several quite narrowing quantum wells in which the ground states are raised. When the operating bias is reached, the ground states form “minibands,” the lowest state of the pre-minibands is appointed as the upper laser state, and the topmost state in the down-minibands is set as the lower laser state. The electrons are inverted between them and perform the THz photon radiation. Owing to the tight couplings inside the miniband areas (by intra-miniband scattering), electrons always relax quickly to the bottom of the minibands, where the upper laser state is located, the upper laser state is filled, and the lower laser state is depopulated. b) *Bound-to-continuum (BtC)*: As shown in **Figure 3b**, this scheme also employs minibands, and the lower laser state is depleted by intra-miniband scattering, similar to the CSL scheme. The main difference

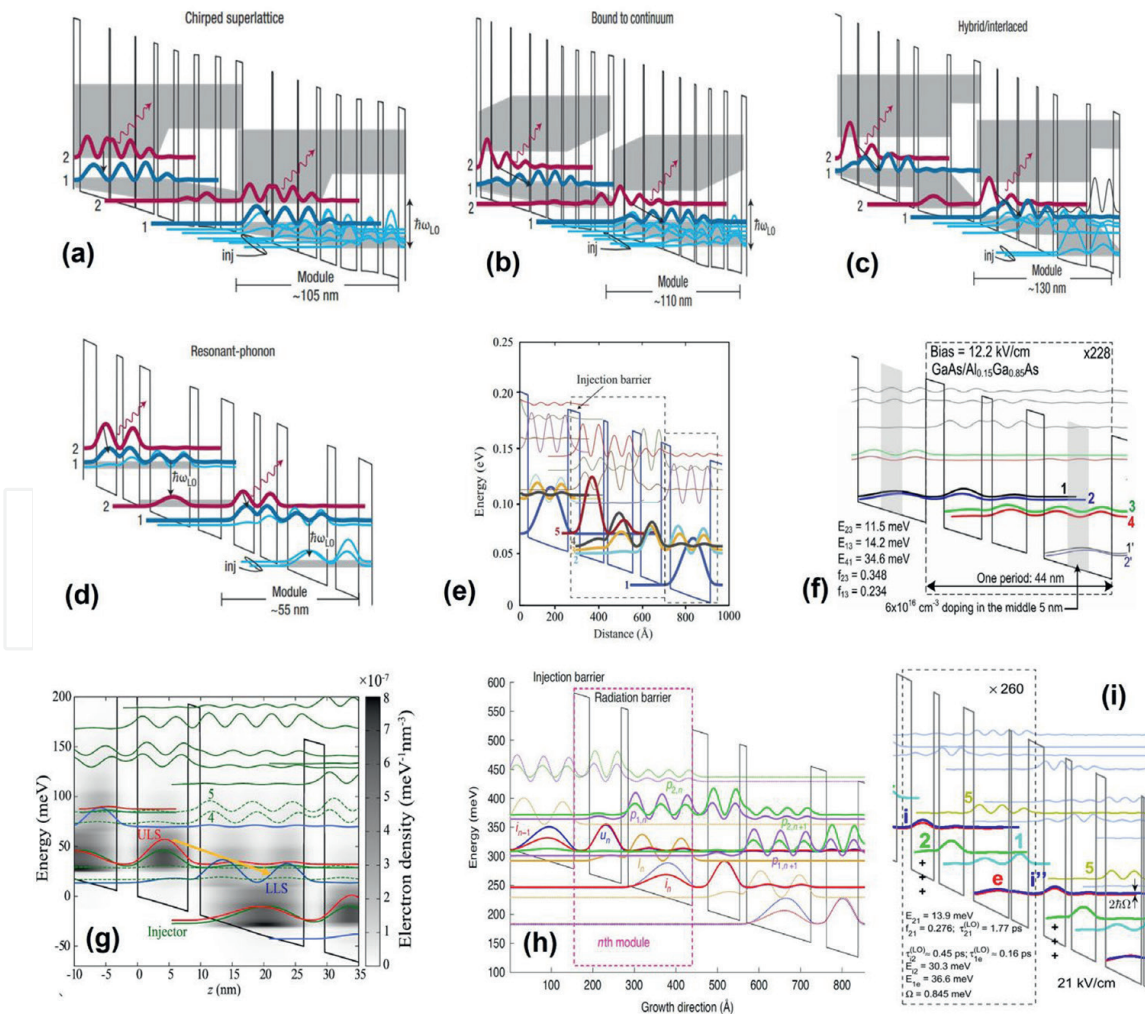


Figure 3. Conduction-band and wavefunctions of each state for different representative THz-QCL design. (a) CSL; (b) BtC; (c) hybrid BtC; (d) one-well injector RP, that permitted from Ref. [34]. (e) two-well extractor RP, from Ref. [35]. (f) three-well RP, from Ref. [36]. (g) and (h), two-well RP, from Ref. [37] and [38]; (i) SA from Ref. [39].

is in the upper-lower state, where it is positioned diagonally with a lower laser state. This diagonality of radiative transition contributes to an increase in the lifetime of the upper laser state and weakens the parasitic overlap of the wavefunctions between the injector and the lower laser state. Therefore, the BtC design displays an improved T_{\max} and output power compared with the CSL design. In addition, an improved BtC scheme with hybrid structures is proposed in which the phonon-assisted depopulation has been incorporated into the miniband areas, which can further relax the thermal backfillings and further improve T_{\max} (**Figure 3c**). c) *Resonant-phonon (RP)*: This scheme is specifically indicated for designs in which the injector follows the resonant tunneling mechanism based on a double-level alignment under operating bias. The depopulation process employs LO-phonon resonance, which mostly takes place intra-well. Therefore, the electrons in the lower laser state are scattered down to the injector states by emitting LO-phonons in the sub-picosecond range. There are several RP schemes with different purposes; for example, the one-well injector RP scheme for better injection selectivity by reducing the direct parasitic overlapping between the injector and the lower laser state (**Figure 3d**), or a two-well extractor RP scheme that is similar to the hybrid BtC for offering more tunneling freedom on the design parameters (**Figure 3e**). The first milestone on T_{\max} is based on a three-well (4-state) RP scheme (**Figure 3f**), including an adjoining-well resonant-tunneling injection and a one-well extractor where its 1st excited state forms resonance alignment with the lower laser state first, and significantly delocalizes the wavefunction of this lower laser state into the extractor well. Consequently, the lower laser state can form strong coupling with the next injector state with one LO phonon energy downward. The further renewed T_{\max} is also based on RP, but with further simplified quantum structures from three-well to two-well (4-state to 3-state, as shown in **Figure 3g** and **h**), where the depopulation from the lower laser state follows only one step via direct intra-well LO phonon scattering. d) *Scattering-assisting (SA)*: As shown in **Figure 3i**, scattering-assisting design is another important scheme. The main difference between SA scheme and the RP design is the injector region, where the SA employs LO-phonon scattering instead of alignment resonance. Resonant tunneling injection always leads to most electrons waiting at the injector before being injected into the upper laser state. Ideally, in the coherent transport regime of resonant tunneling, the upper laser state holds the same number of electrons as the injector state, which is half of the total available population in each period (i.e., a maximum of 50% share in the upper laser state). Owing to the thick injector barrier and the presence of multiple scattering channels, the population share in the upper laser state generally falls below 50%, even at low temperatures. In the SA scheme, by designing the injector to lie one LO-phonon energy up to the upper laser state, this injection limitation can be completely removed.

3. Active-region design by narrowing the period length

Recalling past designs with improved T_{\max} , there is a general trend toward reducing the number of states per period (in other words, narrowing the period length by employing a simple quantum structure), and the radiation transition in the active region is strongly diagonal. As shown in **Figure 4**, we followed the structures calculated in Ref. [37] but recalculated them based on our nonequilibrium Green's function (NEGF) model, that is, two-well RP [37, 38], three-well RP [36], four-well SA [39], four-well BtC [35], and seven-well BtC [40]. This indicates an increasing population share in the upper laser state as the total number of states per period is reduced,

and the optical gain (the peak) at high temperatures is also significantly improved. Therefore, it provides evidence of the potential of a simplified state system based on the RP scheme. The two-well RP is further optimized by relaxing the shortcomings in its antecessor design of the three-well RP, a) *the two-well RP only uses the resonant tunneling process once at the injector*. Even though three-well RP has been well studied and gives the best $T_{\max} \sim 200$ K, a major shortcoming in this scheme is the strict requirement for double resonance alignments at both the injector and extractor region when the bias reaches up to the operating condition. Such a condition is not easy to satisfy in real growth for two reasons. The first reason is the doping issue. High- T_{\max} designs generally employ strong diagonality in the active region, where the suitable oscillator strength for radiation transition is only 0.25–0.35. Because the optical gain is linearly related to this strength ($g \propto f$), this small strength should be compensated for by increasing the average doping levels [41]. In THz-QCLs, the dopant position is always selected far away from the radiation area and is generally at the center of the lower well with a doping length of only several nanometers for restraining the dopant migration into the superlattice interfaces. However, this local heavy doping can give rise to severe band bending as a result of space charges, thereby breaking the resonance alignment conditions. Second, active-region growth is based on molecular beam epitaxy (MBE). Although precise atomic controls have been achieved, it is still quite challenging to obtain thousands of thin quantum wells/barriers where the thickness of each layer is only several nanometers, and the percentage variation in the growth rate over the whole growth time (>10 h) can further worsen the double alignment condition [42]. In addition, the optical gain profile can be broadened and deformed because the applied bias can closely affect the couplings in the active region; thus, the exact laser frequencies suffer from uncertainties [21]. b) *The depopulation in a two-well RP follows an intra-well direct-phonon scattering*. The intra-well

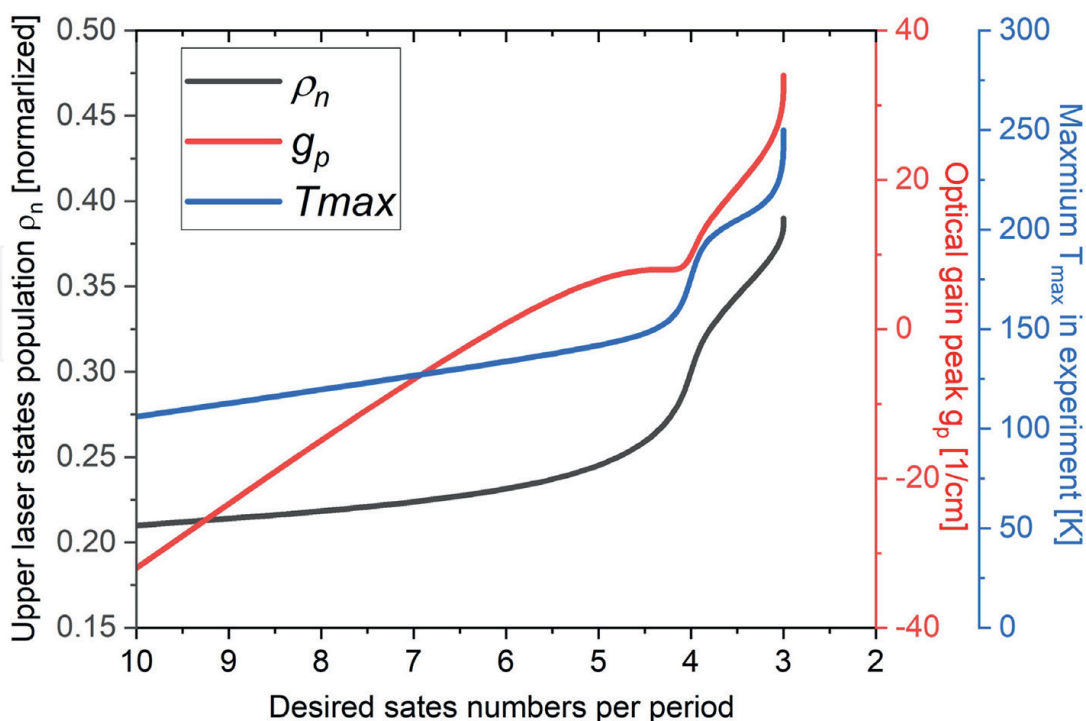


Figure 4.

Calculated population share the upper-laser state (ρ_n), the calculated optical gain peak g_p , and the T_{\max} in experiments. The calculations are based on the designs of two-well (3-state) RP [37, 38], three-well (4-state) RP [36], four-well (4-state) SA [39], and four-well (5-state) BtC [35], seven-well (10-state) BtC [40].

resonance phonon scattering is performed between its 1st excited and ground states in the lower-well, and there is a very strong coupling between them that guarantees a highly efficient depopulation within ultrafast times. Although the energy separation between them can affect depopulation efficiency, it maintains high robustness over a large tuning range of energy separation (30~60 meV [43]). c). *The barriers in two-well RP are much taller.* The tall barrier, by using Al_{0.25}Ga_{0.75}As [37] and Al_{0.3}Ga_{0.7}As [38], can confine the electrodes deeply at the desired states; thus, suppressing the carriers leaking from the confined states over the barriers into the continuum at high temperatures. In a tall barrier design case, careful quantum structure engineering for clean n-clean systems can further minimize the thermal up-scattering from the desired states into the high-lying nonrelevant states. d). *The two-well RP intentionally uses larger depopulation energy for the LO-phonon resonance.* The depopulation energy at the extractor in the high-T_{max} two-well RP is 42 meV in Ref. [37] and 52 meV in Ref [38], which is higher than the previous designs with that exactly equal to one LO-phonon of 36 meV. Although Ref. [38] emphasized the benefits of nonrelevant high-confined state engineering, the contribution of the higher depopulation energy to suppress thermal backfilling is at least equal. In addition to the RP scheme, the narrow-period concept is also attractive for the SA scheme; however, the SA scheme based on a two-well structure has still not been realized in experiments.

4. Limitations in narrow-period active-region design (RP and SA scheme)

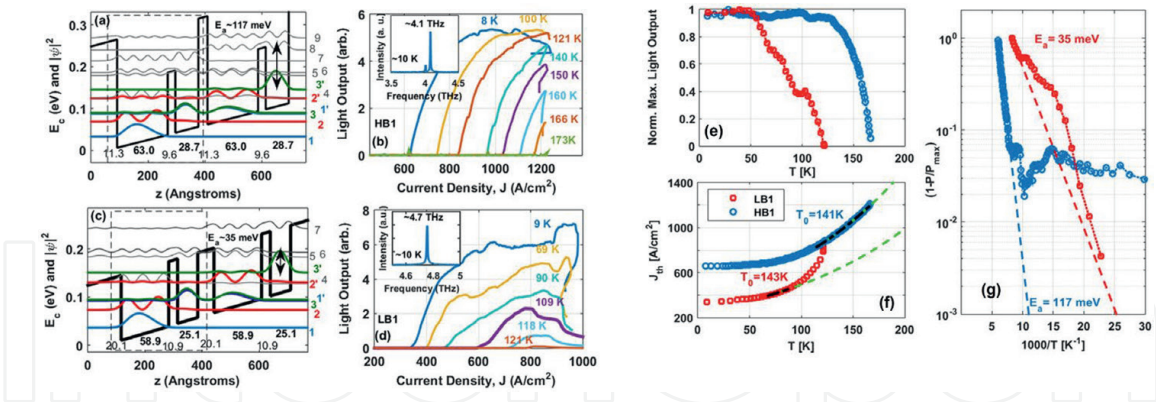
4.1 Two-well RP design

4.1.1 Intra-period thermal up-scattering via non-relevant states

The significance of the high-lying nonrelevant states on high-T_{max} has been demonstrated [19, 20, 44] and indicates that the up-scatterings that originate from the upper laser state into those nonrelevant states in the same period will play a significant role at high temperatures. The up-scattering activation energy E_a was extracted by fitting the Arrhenius plots from the measured device output power by [44]:

$$\ln\left(1 - \frac{P_{out}(T)}{P_{out(max)}}\right) \approx \ln(a) - \frac{E_a}{KT} \quad (1)$$

As shown in **Figure 5**, an E_a of 35 meV is extracted, which presents the thermal up-scattering occurring between the upper laser state and the 1st nonrelevant in the lower well (the 2nd excited state from this well). Following this up-scattering channel, owing to the relatively low activation energy, as the temperature increases, the electrons can escape into the continuum quickly because this nonrelevant state is close to the continuum, which results in a sharp increase in J_{th} at temperatures above 100 K (**Figure 5f**). Therefore, a tall barrier is essential to confine the up-scattered electrons deeply or to increase the up-scattering activation energy. The validity of a tall barrier for suppressing such channels is shown in **Figure 5f** and **g** (As_{0.15}Ga_{0.85}As → Al_{0.3}Ga_{0.7}As), where a much higher up-scattering activation energy is extracted, that is, 35 → 117 meV. The corresponding J_{th} is much lower at high temperatures, and T_{max} improves from 121 to 173 K.

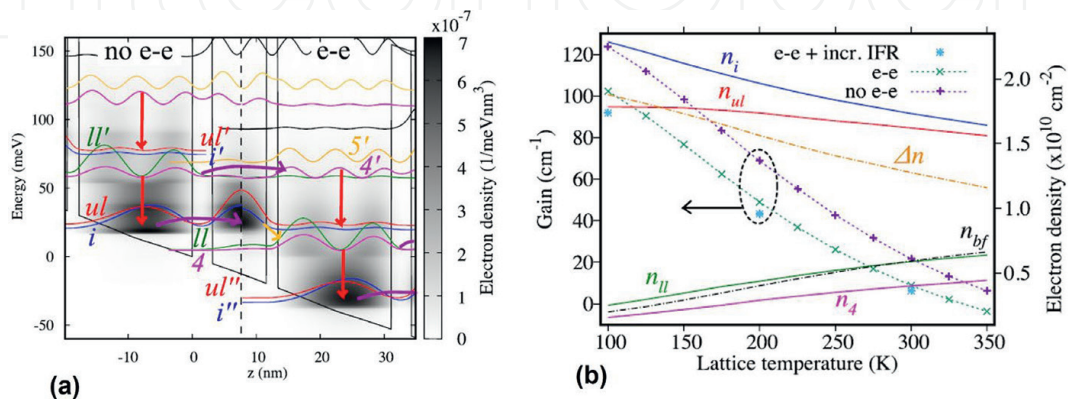

Figure 5.

Band diagram of the two-well RP design by tuning the barrier height. The corresponding light output at different temperatures are shown (a–d). The Arrhenius plots with the fitting activation energy and the J_{th} depending on the temperature is also shown (e–g), Ref. [44].

4.1.2 Depopulation energy and thermal backfilling

Ref. [45] shows that at high temperatures, the thermal backfilling from the injector into the lower-laser state is the main source of the population in the lower-laser state; therefore, dramatically reducing the population inversion. The thermal backfilled electrons (n_{bf}) approach 20% of the population share at 300 K, as shown in **Figure 6a** and **b**, which almost equals to the population of the upper-laser state population; thus, non-inversion can be formed. There are two reasons for this: First, the RP scheme relies on resonant tunneling for electrons injected from the injector, where most of the population resides at the injector; therefore, playing the role of an electron pool for thermal backfilling. Second, the GaAs material has a small LO-phonon of 36 meV. The RP design normally uses depopulation energy that is equal to one LO-phonon; this inherently small depopulation energy encourages the occurrence of thermal backfilling. This also indicates the significance of exploring large LO-phonon energy materials such as GaN [46] and ZnO [47] to suppress thermal backfilling.

If the designs are still based on the GaAs material, enlarging the depopulation energy is an effective method for suppressing the thermal backfilling, and large depopulation energy can further reduce the parasitic coupling of the upper-laser state


Figure 6.

Band diagram in two-well RP design where the population distribution at each state is given at high temperatures (a); The thermal backfilled population from the injector into the lower-laser state (n_{bf}) is particularly (b), Ref. [45].

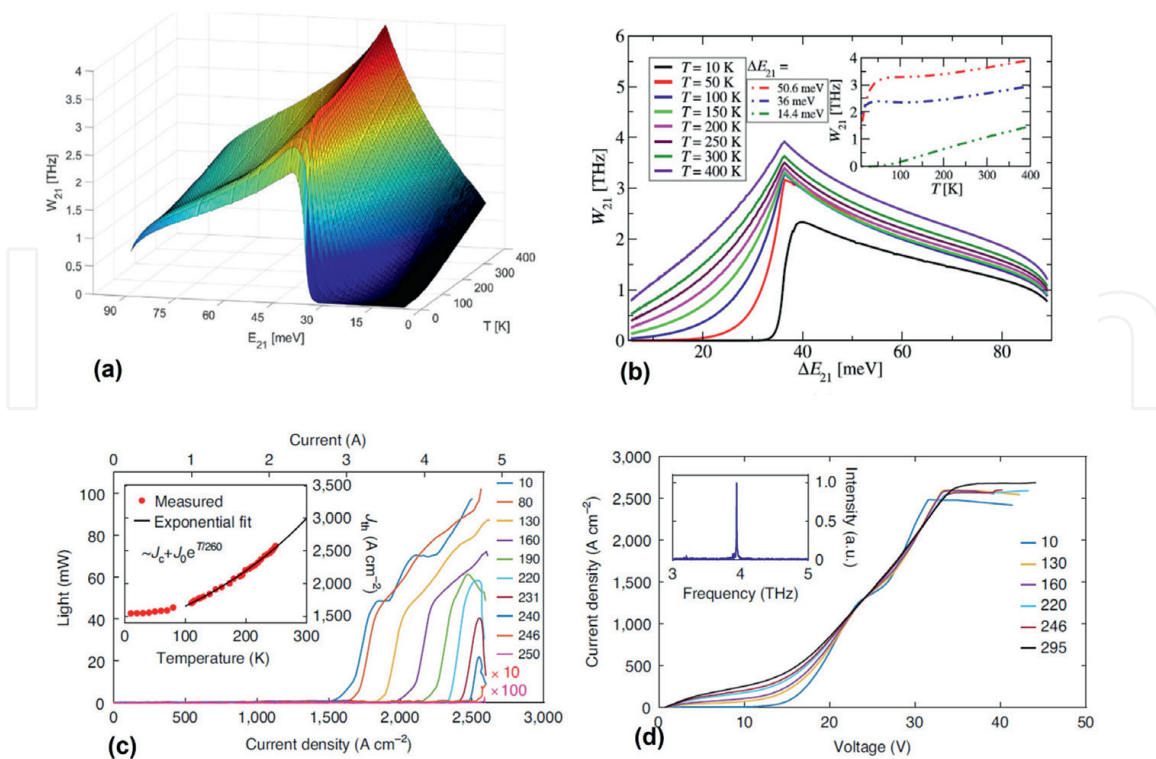


Figure 7. Averaged electron-LO phonon scattering rate between the 1st excited state and the ground state by varying the energy separation between them (a); A representative cross-section of the figure a (b), Ref. [43]; Plot of light output versus current density at different temperatures. Inset: plot of threshold current density versus temperature ($J_{th}-T$) with J_c and J_o as fitting parameters. The black line is an exponential fit (c); Plot of voltage versus current density ($J-V$) at different temperatures. Inset: a lasing spectrum taken at 246 K (d), Ref. [38].

directly with the next injector; therefore, protecting the lifetime of the upper-laser state by preventing parasitic LO-phonon scattering between them. However, the depopulation energy deviating from one LO-phonon slows down the depopulation process, thus increasing the lifetime of the lower-laser state and reducing the population inversion. Ref. [43] estimated the average scattering rate for intra-well LO phonon resonance between the 1st and 2nd states in a single well based on a self-consistent Schrödinger–Poisson solver (**Figure 7a** and **b**). The exact energy separation between them was tuned by varying the well width. It is evident that at a high temperature of 300 K, the depopulation efficiency (here simply assumed by the scattering rate) is reduced by 33% when large depopulation energy of 60 meV is selected. Considering the highest T_{max} in Ref. [38] (**Figure 7c** and **d**), they employed a larger depopulation energy of 52 meV and the improved characteristic temperature of J_{th} in this Ref. was also largely ascribed to the suppression of thermal backfilling, together with the thermal up-scatterings via high-lying nonrelevant states.

4.1.3 Interperiod interactions via nonrelevant states

The two-well configuration inherently has a narrow period length such that the parasitic interactions in neighboring periods can be more serious than in the wide-period design. Furthermore, a narrow period also leads to a stronger electrical field that will lower the nonrelevant states in energy downstream. Ref. [48] addresses the critical effect of nonrelevant high-lying nonrelevant states on the laser threshold current by forming a resonant-tunneling-like channel between three neighboring periods. The

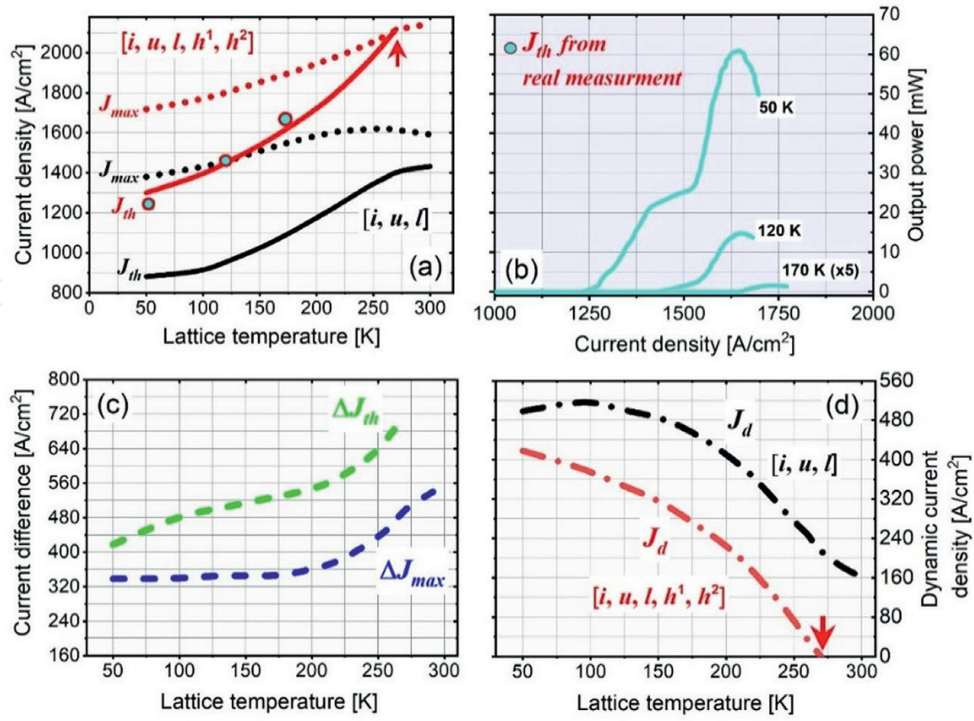


Figure 8. J_{max} and J_{th} depend on the temperatures for only desired states $[i, u, l]$ (black curves) and more high-lying nonrelevant states $[i, u, l, h^1, h^2]$ (red curves) (a); The light output measured devices based on this 2-well RP design. The J_{th} at different temperatures are extracted from those lasing curves and are shown in figure a (b); The changing magnitude of J_{max} and J_{th} (ΔJ_{max} , ΔJ_{th}) by including or excluding the nonrelevant states in the calculations (c); The laser dynamic of J_d depending on the temperatures in both the states inclusion (d), Ref. [48].

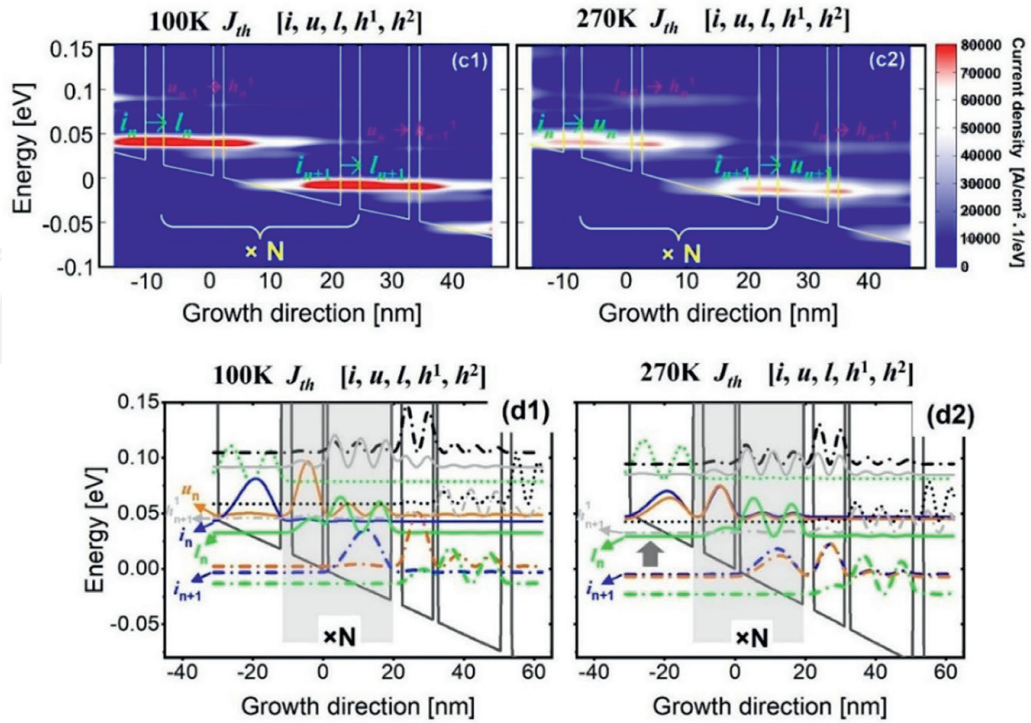


Figure 9. Threshold current J_{th} mappings that resolved by growth direction and energy at both low and high temperatures (100 K, 270 K) for the desired states $[i, u, l]$ and more high-lying nonrelevant states included $[i, u, l, h^1, h^2]$, Ref. [48].

laser dynamics in current will significantly shrink to zero even at 270 K (**Figure 8**). The spatial and energy-resolved current mapping between the neighboring periods clearly shows the tunneling current along the growth directions (**Figure 9**).

4.2 Two-well SA design

4.2.1 More serious inter-period interactions via irrelevant states

The two-well configuration for the SA scheme shows the main difference is that its upper-well is wider for an intra-well LO-phonon scattering injection, and its lower-well is also wide enough to ensure the lower-laser state down to the upper laser state for THz radiation. Therefore, the high-lying nonrelevant states in the lower well were inherently low in energy, as shown in **Figure 10a**. The current-voltage plots in **Figure 10b** show that, at the operating bias, the peak current increases appreciably when both nonrelevant states 4 and 5 are allowed in the calculation. The inclusion of more high-energy states (nonrelevant states 6, 7, and 8) increases the current density further, but only slightly. Therefore, nonrelevant states 4 and 5, which belong to different neighboring periods, are crucial for serious current leakage. It is visible in the spatial and energy resolved current density mappings in **Figure 10c** (A, B, C, D), and the leakage channel is formed due to a strong interaction of the upper-laser states in the upstream period (state $2n_{-1}$) with state 4_n in period n and sequential tunneling to state 5_{n+1} in the downstream period $n+1$ because three of these states are close both in energy and space.

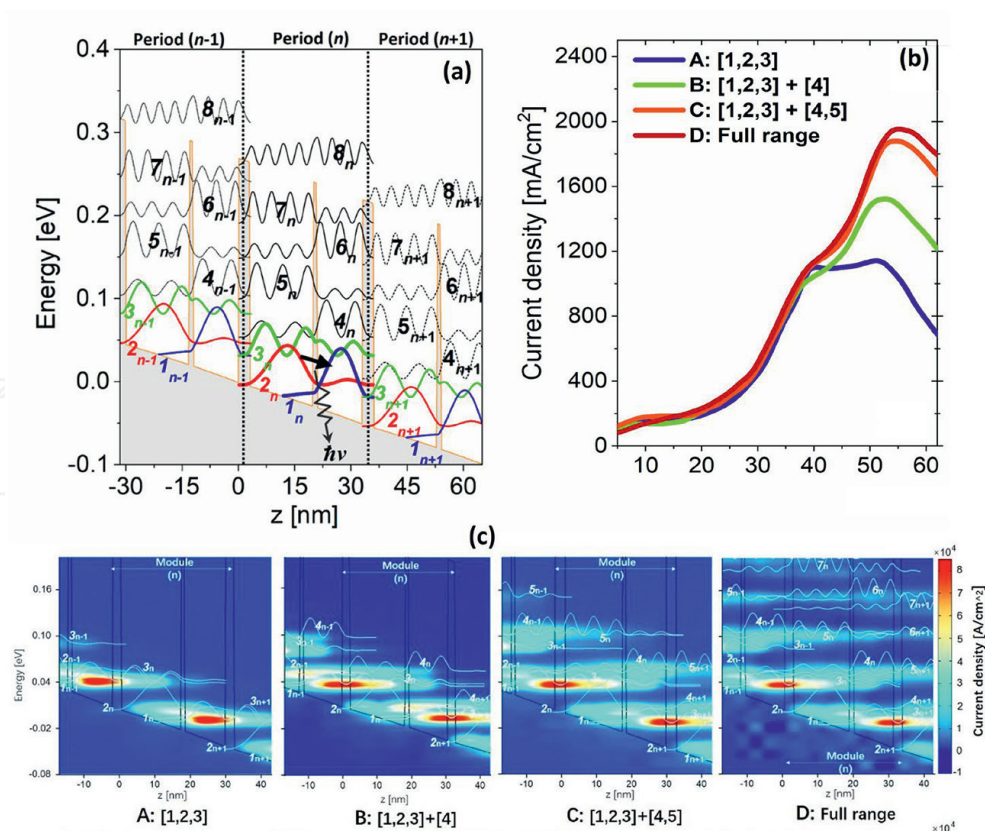
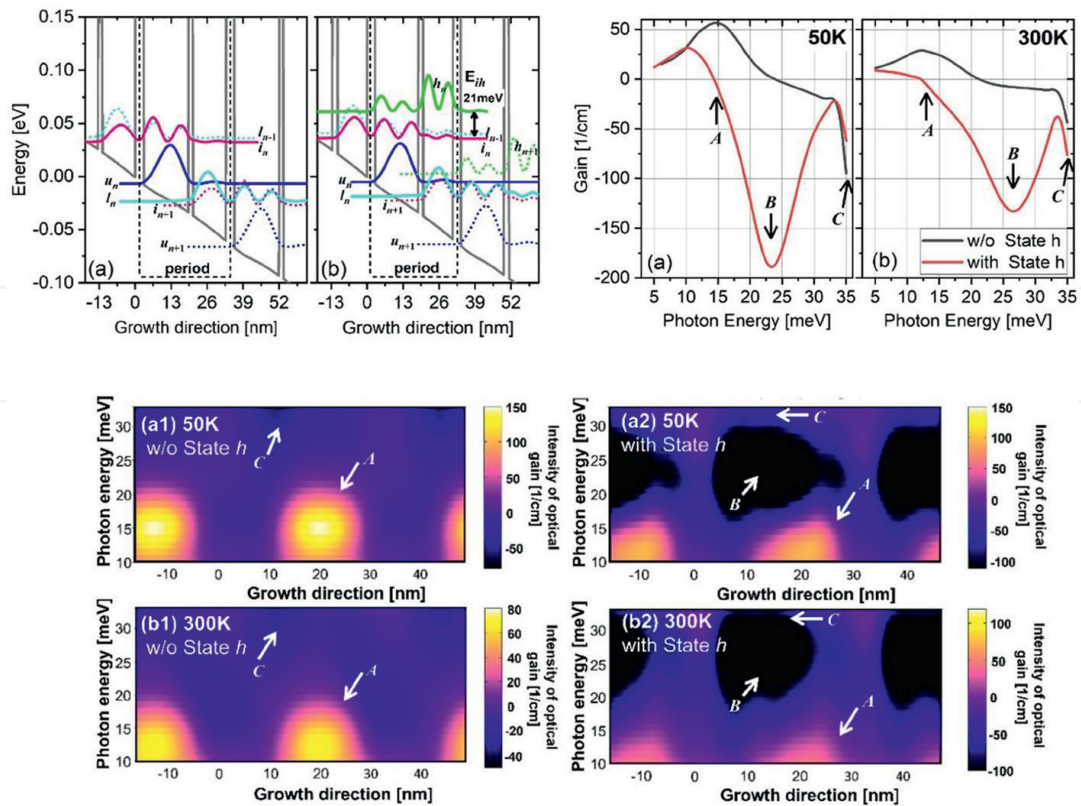


Figure 10. Conduction band diagram and the tight-binding states of two-well SA design with three neighboring periods ($n-1, n, n+1$) (a); The voltage-current plots at high temperatures of 300 K when the different number of the high-lying nonrelevant states are included for calculations (b); The current mapping resolved by the growth direction and the energy when the nonrelevant states are included (c), Ref. [49].


Figure 11.

Band diagram of the two-well SA design in cases of the desired states and the critical nonrelevant state. The optical gain spectra under two different number of stated inclusions. The spatial and energy resolved gain clearly shows the overlapping of the parasitic absorption and the gain area, Ref. [50].

4.2.2 Parasitic absorption overlapping gain

In the two-well SA design (**Figure 11**), there is a strong decoupling between population inversion and optical gain, in which the population inversion does not change significantly when the high-lying nonrelevant states are included, but the peak of gain is significantly limited by those high-lying states. The reduction of the gain peak is obvious at a low temperature of 50 K. This was ascribed to the emergence of inter-period parasitic absorption, which was caused by transitions between the injector and the first nonrelevant states in the lower well (**Figure 11**). This parasitic absorption unavoidably overlaps with the optical gain due to the engineering limit permitted in a simple quantum structure. This overlap was more severe when the lasing frequency exceeded 3 THz in the two-well SA design.

5. Further narrow-period designs

5.1 Split-well three-state RP design

The split-well direct-phonon concept described in Ref. [51] was proposed by using only the ground states to push up the nonrelevant states for a clean-state system, while keeping the depopulation energy almost equal to 36 meV for ultrafast extraction. In this design, each period contained three wells and employed the ground states in each well. Due to all three wells being narrow, the total periodic length is still quite

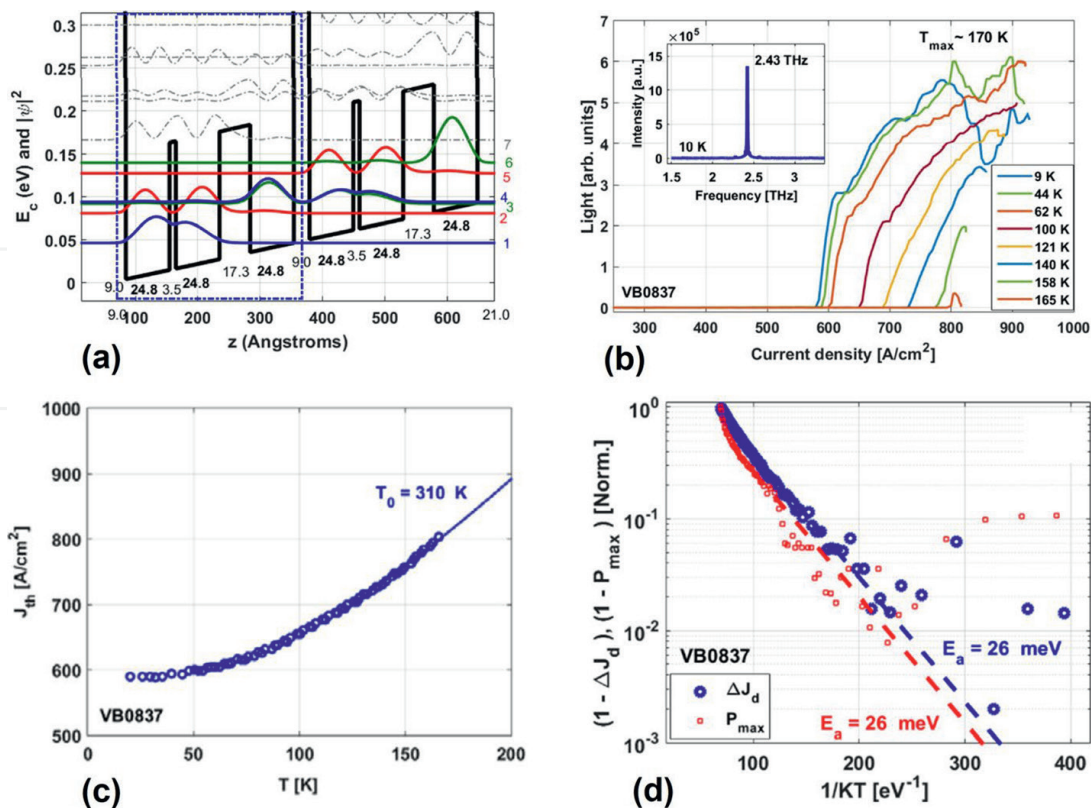


Figure 12. Band profile and the wavefunctions in the “split-well” design (a); Pulsed light output versus current measurement (b); The threshold current vs temperature (c); Activation energy extracted from the laser’s maximum output power (P_{max}) vs temperature, and the current dynamic range $\Delta J_d = (J_{max} - J_{th})$ vs temperature (d), Ref. [51].

small as a “narrow-period” design. Compared with the “all-ground” design from Ref. [52], the main advance in this split-well design is the very strong depopulation couplings between the lower-laser state and the injector, where the “all-ground” design follows a diagonal depopulation process and suffers from limited laser dynamics. As shown in **Figure 12**, the results demonstrate that “split-well” lasers profit from both eliminations of up-scatterings via high-lying nonrelevant states and resonant depopulation of the lower laser states. A negative differential resistance was observed at room temperature beyond the operating bias conditions, indicating that the state system performs as a clean 3-state system, where a high characteristic temperature of J_{th} is fitted out. However, the difficulty of this design is that the splitting at the extractor closely relies on the alignment, and the ultrathin extractor barrier, which is only 3.5 monolayer, is not easily obtained consistently during the long-time MBE growth.

5.2 Two-well double-phonon RP designs

The design in Ref. [53] mainly considers the effect of thermal backfilling on the lower-laser state by using large depopulation energy of more than one LO phonon. This is different from previous designs; the lower-laser state is appointed by the 2nd excited state in the lower well. Simultaneously, the 1st excited state from the lower well is also a depopulation destination, and as a result, three transitions are responsible for the depopulation, that is, $3 \rightarrow 2$, $3 \rightarrow 1$, and $2 \rightarrow 1$, as shown in **Figure 13a**. The tuning of the energy separation between 3 and 2, E_{32} , and also between 2 and 1, E_{21} , was studied, revealing that only by maintaining the total energy separation

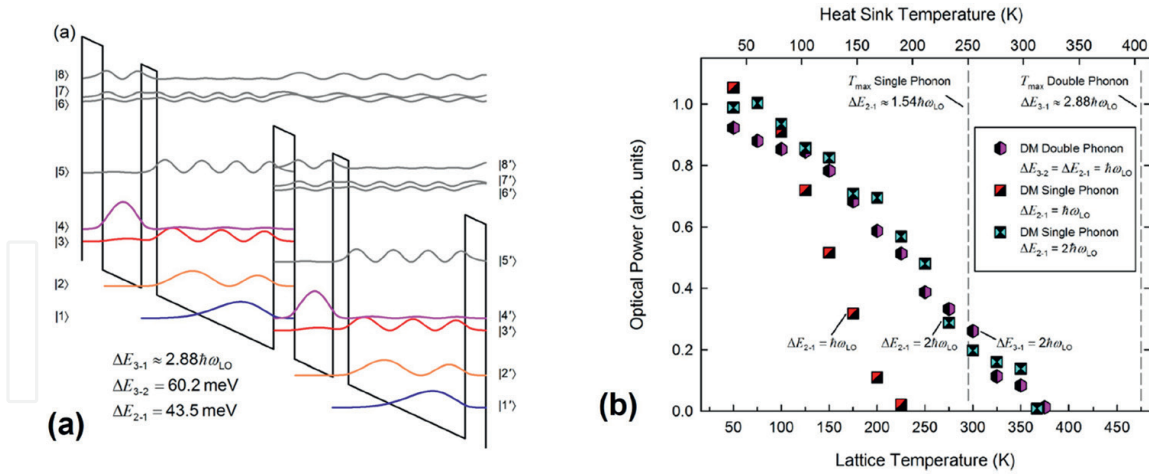


Figure 13. Conduction band diagram and the wavefunctions in a double phonon intrawell depopulated based on a two-well structure (a); The calculated optical output versus temperature by tuning the depopulation energy with single- and double-phonon (b), Ref. [53].

between the lower laser state and the next injector, E_{31} , more than a double phonon, the thermal backfilling can be well suppressed and thus shows a cut-off temperature above 300 K (**Figure 13b**). The challenge with such large depopulation energy is that it requires a much taller barrier, and the operating electric field is very strong, which causes many difficulties in device realization.

5.3 Two step-well SA design

As described above, in a two-well SA design, the high-lying nonrelevant state (the 1st excited state in the lower well), h , as shown in **Figure 14a**, is naturally close to the desired states and forms a serious parasitic absorption overlapping the gain

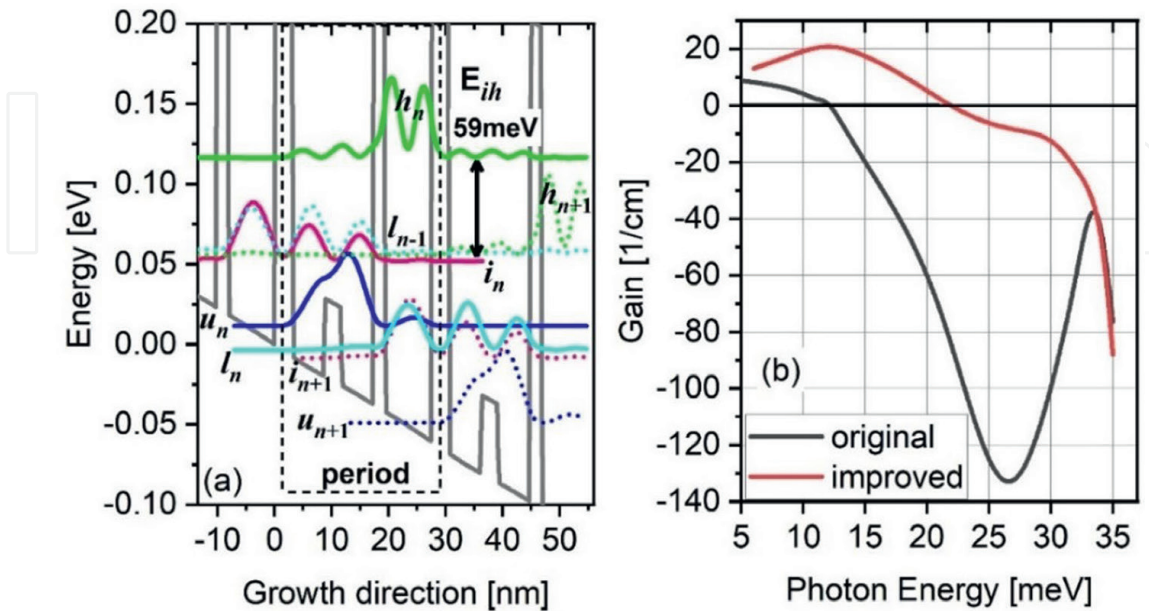


Figure 14. Improved two-well SA design by employing ministepped ($Al_{0.05}Ga_{0.95}As$) where the tall barriers of $Al_{0.05}Ga_{0.95}As$ are used (a); Comparison of optical gain spectra at 300 K in this improved design (red curve) and the regular two-well SA design. Both spectra are predicated by considering the high-lying nonrelevant states (u, l, i, h) (b), Ref. [50].

areas. Consequently, the peak gain was largely limited even at low temperatures. Ref. [50] attempted to narrow the upper well, where the lower well can be correspondingly narrower. Therefore, the irrelevant state h moves upward. To satisfy the energy separation between injector states i and the upper laser state u close to the LO-phonon, a ministep was intentionally introduced into the upper well. By simply tuning this ministep, the energy separation of the injector state i and the upper-laser state u can be maintained at 36 meV. To achieve the same THz frequency of 3.7 THz, the upper well is narrowed by 13% compared with the regular two-well SA design (16.2→14.2 nm), and the lower well is also narrowed by 33% (10.6→8.18 nm). The irrelevant state h is thus effectively moved upward, and the energy separation E_{ih} is significantly increased from 21 to 59 meV. The optical gain spectra in **Figure 14b** show complete suppression of overlapping from this parasitic absorption and recovery of the peak gain.

6. Strict request on MBE growth controls for the narrow-period designs

The simple structure requires more precise control of the growth because each layer performs multiple functions as the design parameters. The recent highest T_{\max} emphasizes high-quality growth on repeating periods and interfaces. It is very challenging to grow thin layers, especially in the case of tall barriers with several monolayers. The interface flatness, doping controls, and the period repeated during the long-time growth are tough topics for start-of-art designs. Meanwhile, uniformity across a 3-inch substrate is also critical, even for optimizing the rotations carefully, and an arbitrary thickness error can still be approximately 2%. Reliable and repeatable growth is essential for dedicated design parameters for a higher T_{\max} (i.e., even within a very small range of parameter balances in such designs).

7. Summary

Despite the extensive application potential of the THz spectrum, light radiation sources remain the most urgent, where the most expected is a compact solid-state device analogous to conventional semiconductor lasers. The THz quantum cascade laser has been treated as the most attractive candidate to fill the THz gap and was soon realized in the THz range after the experimental demonstration in the mid-infrared range. However, this type of THz laser suffers from thermal degradation that cannot work at room temperature until now. Different models attempt to describe the quantum transport in THz-QCLs and clarify the thermal limitations, then predict the designs with high-temperature tolerances. The design for high-temperature operation follows a path by simplifying the containing quantum well structure in each period; however, such a narrow period requires careful engineering of the barrier and requires the control of the high-lying nonrelevant states to suppress any inter-period parasitic channels (for example, creating a clean state system). Different strategies are needed depending on the injection method (resonant tunneling method or scattering-assisted method). In addition, to realize these narrow-period structures, precise control of the MBE growth is essential to ensure the accurate thickness of each layer and the flatness of interfaces with uniform alloyed barriers.

IntechOpen


IntechOpen

Author details

Li Wang* and Hideki Hirayama
Research Center for Advanced Photonics, RIKEN, Sendai, Japan

*Address all correspondence to: li.wang@riken.jp

IntechOpen

© 2022 The Author(s). Licensee IntechOpen. This chapter is distributed under the terms of the Creative Commons Attribution License (<http://creativecommons.org/licenses/by/3.0>), which permits unrestricted use, distribution, and reproduction in any medium, provided the original work is properly cited. 

References

- [1] Mittleman DM. Twenty years of terahertz imaging. *Optics Express*. 2018;**26**:9417-9431
- [2] Siegel PH. Terahertz technology. *IEEE Transactions on Microwave Theory and Techniques*. 2002;**50**:910-928
- [3] Korter T, Plusquellic DF. Continuous-wave terahertz spectroscopy of biotin: Vibrational anharmonicity in the far-infrared. *Chemical Physics Letters*. 2004;**385**:45-51
- [4] Ogawa Y, Hayashi S, Oikawa M, Otani C, Kawase K. Interference terahertz label-free imaging for protein detection on a membrane. *Optics Express*. 2008;**16**:22083-22089
- [5] Kohler R, Tredicucci A, Beltram F, Beere HE, Linfield EH, Davies AG, et al. Terahertz semiconductor-heterostructure laser. *Nature*. 2002;**417**:156-159
- [6] Williams BS, Callebaut H, Kumar S, Hu Q, Reno JL. 3.4-THz quantum cascade laser based on longitudinal-optical-phonon scattering for depopulation. *Applied Physics Letters*. 2003;**82**:1015-1017
- [7] Luo H, Laframboise SR, Wasilewski ZR, Aers GC, Liu HC, Cao JC. Terahertz quantum cascade lasers based on a three-well active module. *Applied Physics Letters*. 2007;**90**:041112
- [8] Kumar S, Lee AWM. Resonant-phonon terahertz quantum-cascade lasers and video-rate terahertz imaging. *IEEE Journal of Selected Topics in Quantum Electronics*. 2008;**14**:333-344
- [9] Scalfari G, Walther C, Fischer M, Terazzi R, Beere H, Ritchie D, et al. THz and sub-THz quantum cascade lasers. *Laser & Photonics Reviews*. 2009;**3**:45-105
- [10] Callebaut H, Hu Q. Importance of coherence for electron transport in terahertz quantum cascade lasers. *Journal of Applied Physics*. 2005;**98**:104505
- [11] Kohen S, Williams BS, Hu Q. Electromagnetic modeling of terahertz quantum cascade laser waveguides and resonators. *Journal of Applied Physics*. 2005;**97**:053106
- [12] Adam AJL, Kasalynas I, Hovenier JN, Klaassen TO, Gao JR, Orlova EE, et al. Beam patterns of terahertz quantum cascade lasers with subwavelength cavity dimensions. *Applied Physics Letters*. 2006;**88**:151105
- [13] Fan JA, Belkin MA, Capasso F, Khanna S, Lachab M, Davies AG, et al. Surface emitting terahertz quantum cascade laser with a double-metal waveguide. *Optics Express*. 2007;**14**:11672-11680
- [14] Kumar S, Williams BS, Qin Q, Lee AWM, Hu Q, Reno JL. Surface-emitting distributed feedback terahertz quantum-cascade lasers in metal-metal waveguides. *Optics Express*. 2007;**15**:113-128
- [15] Chassagneux Y, Colombelli R, Maineult W, Barbieri S, Beere HE, Ritchie DA, et al. Electrically pumped photonic-crystal terahertz lasers controlled by boundary conditions. *Nature*. 2009;**457**:174-178
- [16] Wen BY, Ban DY. High-temperature terahertz quantum cascade lasers. *Progress in Quantum Electronics*. 2021;**80**:100363
- [17] Albo A, Hu Q. Investigating temperature degradation in THz quantum cascade lasers by examination

of temperature dependence of output power. *Applied Physics Letters*. 2015;**106**:131108

[18] Kumar S, Hu Q, Reno JL. 186 K operation of terahertz quantum-cascade lasers based on a diagonal design. *Applied Physics Letters*. 2009;**94**:131105

[19] Albo A, Hu Q. Carrier leakage into the continuum in diagonal GaAs/Al_{0.15}GaAs terahertz quantum cascade lasers. *Applied Physics Letters*. 2015;**107**:241101

[20] Albo A, Hu Q, Reno JL. Room temperature negative differential resistance in terahertz quantum cascade laser structures. *Applied Physics Letters*. 2016;**109**:081102

[21] Kumar S, Hu Q. Coherence of resonant-tunneling transport in terahertz quantum-cascade lasers. *Physical Review B*. 2009;**80**:245316

[22] Williams BS, Kumar S, Qin Q, Hu Q. Terahertz quantum cascade lasers with double-resonant-phonon depopulation. *Applied Physics Letters*. 2006;**88**:261101

[23] Lü JT, Cao JC. Coulomb scattering in the Monte Carlo simulation of terahertz quantum-cascade lasers. *Applied Physics Letters*. 2006;**88**:061119

[24] Nelander R, Wacke A. Temperature dependence of the gain profile for terahertz quantum cascade lasers. *Applied Physics Letters*. 2008;**92**:081102

[25] Grange T. Contrasting influence of charged impurities on transport and gain in terahertz quantum cascade lasers. *Physical Review B*. 2015;**92**:241306

[26] Banit F, Lee S-C, Knorr A. Self-consistent theory of the gain linewidth for quantum-cascade lasers. *Applied Physics Letters*. 2005;**86**:041108

[27] Kazarinov RF, Suris RA. Possibility of the amplification of electromagnetic waves in a semiconductor with a superlattice. *Soviet Physics – Semiconductors*. 1971;**5**:707-709

[28] Faist J, Capasso F, Sivco DL, Sirtori C, Hutchinson AL, Cho AY. Quantum cascade laser. *Science*. 1994;**264**:553-556

[29] Kumar S, Williams BS, Hu Q, Reno JL. 1.9 THz quantum-cascade lasers with one-well injector. *Applied Physics Letters*. 2006;**88**:121123

[30] Walther C, Scaliari G, Faist J, Beere H, Ritchie D. Low frequency terahertz quantum cascade laser operating from 1.6 to 1.8-THz. *Applied Physics Letters*. 2006;**89**:231121

[31] Walther C, Fischer M, Scaliari G, Terazzi R, Hoyler N, Faist J. Quantum cascade lasers operating from 1.2 to 1.6 THz. *Applied Physics Letters*. 2007;**91**:131122

[32] Williams BS, Kumar S, Hu Q. Operation of terahertz quantum-cascade lasers at 164 K in pulsed mode and at 117 K in continuous-wave mode. *Optics Express*. 2005;**13**:3331-3339

[33] Khanal S, Reno JL, Kumar S. 2.1 THz quantum-cascade laser operating up to 144 K based on a scattering-assisted injection design. *Optics Express*. 2015;**23**:19689-19697

[34] Williams BS. Terahertz quantum-cascade lasers. *Nature Photonics*. 2007;**1**:517-525

[35] Ohtani K, Turčinková D, Bonzon C, Beck M, Faist J, Justen M, et al. High performance 4.7 THz GaAs quantum cascade lasers based on four quantum wells. *New Journal of Physics*. 2016;**18**:12300

- [36] Fatholouloumi S, Dupont E, Chan CWI, Wasilewski ZR, Laframboise SR, Ban D, et al. Terahertz quantum cascade lasers operating up to ~200 K with optimized oscillator strength and improved injection tunneling. *Optics Express*. 2012;**20**:3866-3876
- [37] Bosco L, Franckić M, Scaliari G, Beck M, Wacker A, Faist J. Thermoelectrically cooled THz quantum Cascade laser operating up to 210 K. *Applied Physics Letters*. 2019;**115**:010601
- [38] Khalatpour A, Paulsen AK, Deimert C, Wasilewski ZR, Hu Q. High-power portable terahertz laser systems. *Nature Photonics*. 2021;**15**:16-20
- [39] Razavipour SG, Dupont E, Fatholouloumi S, Chan CWI, Lindskog M, Wasilewski ZR, et al. An indirectly pumped terahertz quantum cascade laser with low injection coupling strength operating above 150 K. *Journal of Applied Physics*. 2013;**113**:203107
- [40] Scaliari G, Hoyler N, Giovannini M, Faist J. Terahertz bound-to-continuum quantum-cascade lasers based on optical-phonon scattering extraction. *Applied Physics Letters*. 2005;**86**:181101
- [41] Chan CWI, Albo A, Hu Q, Reno LJ. Tradeoffs between oscillator strength and lifetime in terahertz quantum cascade lasers. *Applied Physics Letters*. 2016;**109**:201104
- [42] Andrews AM, Zedeerbauer T, Hermann M, MacFarland DS, Strasser G. *Quantum Cascade Lasers, Molecular Beam Epitaxy from Research to Mass Production*. Amsterdam, Netherlands: ScienceDirect Book; 2018. pp. 597-624
- [43] Demic A, Ikonc Z, Dean P, Indjin D. Prospects of temperature performance enhancement through higher resonant phonon transition designs in GaAs-based terahertz quantum-cascade lasers. *New Journal of Physics*. 2022;**24**:033047
- [44] Albo A, Flores YV, Hu Q, Reno JL. Two-well terahertz quantum cascade lasers with suppressed carrier leakage. *Applied Physics Letters*. 2017;**111**:111107
- [45] Frankie M, Bosco L, Beck M, Bonzon C, Mavrona E, Scaliari G. Two-well quantum cascade laser optimization by non-equilibrium Green's function modelling. *Applied Physics Letters*. 2018;**112**:021104
- [46] Wang L, Lin T-T, Chen M-X, Wang K, Hirayama H. Engineering of electron-longitudinal optical phonon coupling strength in m-plane GaN terahertz quantum cascade lasers. *Applied Physics Express*. 2021;**14**:112003
- [47] Bellotti E, Driscoll K, Moustakas TD, Paiella R. Monte Carlo simulation of terahertz quantum cascade laser structures based on wide-bandgap semiconductors. *Journal of Applied Physics*. 2009;**105**:113103
- [48] Wang L, Lin T-T, Wang K, Hirayama H. Nonrelevant quantum levels limited laser dynamic in narrow-period terahertz quantum cascade lasers Li Wang. *Japanese Journal of Applied Physics*. 2022
- [49] Wang L, Lin T-T, Wang K, Grange T, Birner S, Hirayama H. Short-period scattering-assisted terahertz quantum cascade lasers operating at high temperatures. *Scientific Reports*. 2019;**9**:9446
- [50] Wang L, Lin T-T, Wang K, Hirayama H. Limitation of parasitic absorption in designs of three-state terahertz quantum cascade lasers with direct-phonon injection. *Applied Physics Express*. 2022;**15**:052002

[51] Albo A, Flores YV, Hu Q, Reno JL. Split-well direct-phonon terahertz quantum cascade lasers. *Applied Physics Letters*. 2019;**114**:191102

[52] Chan CWI, Hu Q, Reno JL. Ground state terahertz quantum cascade lasers. *Applied Physics Letters*. 2012;**101**:151108

[53] Freeman W. Double longitudinal-optical phonon intrawell depopulated terahertz quantum cascade structures: Electron transport modeling using a density matrix method. *Applied Physics Letters*. 2021;**118**:241107

IntechOpen